

# Switching interlayer magnetic order in bilayer CrI<sub>3</sub> by stacking reversal

Xiangru Kong,<sup>1,\*</sup> Hongkee Yoon,<sup>2,\*</sup> Myung Joon Han,<sup>2,†</sup> and Liangbo Liang<sup>1,†</sup>

<sup>1</sup>Center for Nanophase Materials Sciences, Oak Ridge National Laboratory (ORNL), Oak Ridge, Tennessee 37831, USA

<sup>2</sup>Department of Physics, Korea Advanced Institute of Science and Technology (KAIST), Daejeon 34141, Republic of Korea

CrI<sub>3</sub>, a hot two-dimensional (2D) magnet, exhibits complex magnetism depending on the number of layers and interlayer stacking patterns. For bilayer CrI<sub>3</sub>, the interlayer magnetism can be tuned between ferromagnetic (FM) and antiferromagnetic (AFM) order by manipulating the stacking order. However, the stacking is mostly modified through translation between the layers, while the effect of rotation between the layers on the interlayer magnetic order has not yet been fully investigated. Here, we considered three energetically stable stacking patterns  $R\bar{3}$ ,  $C2/m$  and AA in bilayer CrI<sub>3</sub>, and the reversed counterparts  $R\bar{3}$ -r,  $C2/m$ -r and AA-r through rotating one layer by 180° with respect to the other layer. Our first-principles calculations suggest that the interlayer magnetic ground state can be switched from AFM to FM (or FM to AFM) by reversing the stacking pattern. A detailed microscopic analysis was carried out by magnetic force theory calculations on  $C2/m$  stacking which favors AFM and  $C2/m$ -r stacking which favors FM. The interlayer magnetic interactions and the origin of the magnetic order change were revealed through specific orbital analysis. Our work demonstrates that stacking rotation can also tune the interlayer magnetism of CrI<sub>3</sub>, and provides microscopic insight into understanding its interlayer magnetic properties.

**KEYWORDS:** Two-dimensional magnets; CrI<sub>3</sub>; interlayer magnetism; density functional theory; stacking pattern reversal

## I. INTRODUCTION

After the discovery of graphene [1, 2], much attention have been attracted by the two-dimensional (2D) materials due to the reduced dimensionality that could bring about more controllability in promising nano-device fabrications [3]. Soon, researchers began to wonder about the possibility of 2D magnetic materials [4]. Recently, ferromagnetic (FM) monolayer CrI<sub>3</sub> and few-layer Cr<sub>2</sub>Ge<sub>2</sub>Te<sub>6</sub> were successfully discovered in experiments by magneto-optical Kerr effect microscopy [5, 6]. As both CrI<sub>3</sub> and Cr<sub>2</sub>Ge<sub>2</sub>Te<sub>6</sub> are insulators, metallic phase in 2D magnetic monolayer Fe<sub>3</sub>GeTe<sub>2</sub> was also realized by a device fabrication technique [7]. Followed by these seminal works, a 2D topological magnetic material MnBi<sub>2</sub>Te<sub>4</sub> has attracted much attention due to the observation of quantum anomalous Hall effect in its few layers [8]. NiPS<sub>3</sub> is another type of 2D antiferromagnetic insulator that hosts coherent many-body excitons and exhibits novel spin-dependent optical behaviors [9–11]. The outstanding physical properties in 2D magnetic materials and their diverse heterostructures demonstrate the potential values in fundamental research and future applications [12–17]. For example, spin filter devices were proposed in graphite/CrI<sub>3</sub>/graphite magnetic tunnel junctions [18], and Majorana edge modes that can be exploited for topological quantum computations can be realized in the heterostructure consisting of FM monolayer CrBr<sub>3</sub> and superconducting NbSe<sub>2</sub> [19].

The layers of 2D magnetic materials are typically bonded by van der Waals (vdW) forces. The weak vdW interactions and large distances between magnetic ions raise the question of what the interlayer magnetism should be. Confusions initially occurred about the interlayer magnetism in CrI<sub>3</sub> thin

films, particularly the bilayer. Interlayer AFM order in bilayer CrI<sub>3</sub> was experimentally confirmed by magneto-optical Kerr effect measurement [5], tunneling measurement [18, 20] and Raman spectroscopy [21], but interlayer FM order was predicted by first-principles calculations to be energetically favorable in bilayer CrI<sub>3</sub> with the rhombohedral structure (i.e., the  $R\bar{3}$  interlayer stacking pattern) [22–25]. The rhombohedral structure ( $R\bar{3}$  stacking) commonly exists in bulk CrI<sub>3</sub> at low temperature; with temperature increasing to 210–220 K, it undergoes a phase transition to a monoclinic structure with the  $C2/m$  interlayer stacking [26]. The inconsistency between experiments and calculations hinted that bilayer CrI<sub>3</sub> may not possess the same rhombohedral structure ( $R\bar{3}$  stacking) as the bulk at low temperature. Later on, experimental studies by polarization resolved Raman spectroscopy [27–30] suggested that bilayer CrI<sub>3</sub> actually assumes the monoclinic structure ( $C2/m$  stacking) even at low temperature, where interlayer AFM coupling is more favourable according to first-principles calculations [22–25], finally in agreement with the experimentally measured interlayer AFM magnetism. Although  $R\bar{3}$  stacking is more energetically favorable in bilayer CrI<sub>3</sub> compared to  $C2/m$  stacking, bilayer CrI<sub>3</sub> samples exfoliated from  $C2/m$ -stacked bulk samples at room temperature are probably kinetically trapped in the monoclinic  $C2/m$  stacking on cooling from room temperature to cryogenic temperatures, due to the transition barrier of roughly 10 meV/Cr from  $C2/m$  to  $R\bar{3}$  stacking [25] and the encapsulation layers (graphene or hBN) [23, 27]. These results not only prove that first-principles calculations can guide and corroborate experiments, but also demonstrate that the interlayer magnetic order in bilayer CrI<sub>3</sub> can be manipulated by varying the stacking pattern [22–25, 27, 28].

So far, the stacking order of CrI<sub>3</sub> is mostly controlled through translation between the layers ( $R\bar{3}$  and  $C2/m$  stackings can be translated to each other) [23–25], while the effect of rotation between the layers on the interlayer magnetism has not yet been thoroughly investigated [31]. Recently, by

\* These authors contributed equally to this work

† Corresponding authors: mj.han@kaist.ac.kr; liangl1@ornl.gov

molecular beam epitaxy, CrBr<sub>3</sub> bilayers with the top and bottom layers aligned and anti-aligned (or rotated by 180°) were grown, and exhibited opposite interlayer magnetic orders [32]. This motivates us to study how stacking rotation will affect the interlayer magnetism in bilayer CrI<sub>3</sub> and understand why the interlayer magnetic order can change with stacking reversal in Cr-trihalide bilayers. Here, we explored multiple energetically stable stacking patterns in bilayer CrI<sub>3</sub>:  $R\bar{3}$ ,  $C2/m$  and AA [23], and their reversed counterparts:  $R\bar{3}$ -r,  $C2/m$ -r and AA-r via rotating one layer by 180° with respect to the other layer. Utilizing different DFT+ $U$  methods and the hybrid functional approach from first-principles density functional theory (DFT) calculations, we first examined the total energies of these stacking patterns and the corresponding reversed stackings to determine the favored interlayer magnetic groundstate in each stacking. It was found that the magnetic ground state in bilayer CrI<sub>3</sub> can be switched from AFM to FM (or FM to AFM) by reversing the stacking, similar to the experimental findings in bilayer CrBr<sub>3</sub> discussed above [32]. At last, a microscopic explanation of interlayer magnetic interactions and the origin of the magnetic order change with stacking rotation were given by magnetic force theory calculations and detailed orbital analysis.

## II. COMPUTATIONAL METHODS

DFT calculations within the projected augmented wave (PAW) method were carried out in the Vienna *ab initio* simulation package (VASP, version 5.4.4) [33–35]. The electron exchange-correlation functional was chosen as the generalized gradient approximation (GGA) of Perdew, Burke and Ernzerhof (PBE) [36]. The corrections for interlayer vdW interactions were considered by the optB86-vdW method [25, 37, 38]. As checked in Refs. [24, 25], different exchange-correlation functionals and vdW corrections generally bring slight changes to the results and do not alter the magnetic ground states. Therefore, we focus on the PBE functional and optB86-vdW corrections in this work [37, 38]. The structures were fully relaxed by the conjugate gradient scheme until the maximum force was less than 1 meV/Å on each atom. The total energy was converged to 10<sup>-8</sup> eV. The energy cutoff of the plane waves was chosen as 350 eV. The k-mesh in the Brillouin Zone was sampled using  $\Gamma$ -centered 12 × 12 × 1 k-grid. Besides, a vacuum region of about 20 Å in the  $z$  direction was used to avoid spurious interactions with the neighboring cells.

We note that as the localized  $d$  orbitals of Cr atoms contribute to the most density of states near the Fermi level [39], the strong electron correlations effect should be considered by the DFT+ $U$  scheme. Previous studies have showed that the total energy of bilayer CrI<sub>3</sub> is sensitive to the specific DFT+ $U$  implementation formalism and interaction parameters of  $U$  and  $J$  [24, 25]. Therefore, we employed different DFT+ $U$  methods in our work by examining both Dudarev’s approach [40] and Liechtenstein’s approach [41–43], and we considered various  $U$  and  $J$  values used in prior works [23–25]. For Dudarev’s approach, the independent effective on-site Coulomb and exchange parameters  $U$  and  $J$  are not mean-

ingful, since the parameters  $U$  and  $J$  do not enter into the energy term separately; instead, they appear together in the fashion of  $U - J$ , making  $U_{eff} = U - J$  the single effective parameter. In our work,  $U_{eff}$  was taken with values of 2.0, 3.0, 4.0, 5.0 eV ( $U_{eff} = 3.0$  eV was the value adopted by a prior work [23]). As for Liechtenstein’s approach, we need to specify the respective  $U$  and  $J$  values, since they appear in the energy term separately. Here we considered two sets of  $U$  and  $J$  values determined from previous works: one corresponds to  $U = 2.9$  eV and  $J = 0.7$  eV obtained from the constrained random phase approximation (cRPA) [44–48], the values chosen by Ref. [24]; and the other corresponds to  $U = 3.9$  eV and  $J = 1.1$  eV self-consistently calculated based on a linear response method [49], the values used by Ref. [25].

To further verify the magnetic ground state of the stacking patterns in bilayer CrI<sub>3</sub>, the screened Heyd-Scuseria-Ernzerhof hybrid functional (HSE06) method [50, 51] was also considered. The structures (both lattice constants and atomic positions) were fully optimized until the maximum residual force was less than 10 meV/Å, and the total energy was converged to 10<sup>-6</sup> eV. The energy cutoff was still 350 eV. The k-mesh was sampled using  $\Gamma$ -centered 6 × 6 × 1 k-grid.

For the magnetic force theory (MFT) calculations [52–54], we used the OPENMX software package [54, 55], which is based on the linear combination of pseudoatomic orbitals (LCPAO) basis set. The full-band Hamiltonian obtained from OPENMX was used for the magnetic force calculation using our MFT software  $\mathbf{Jx}$  [56, 57]. For both  $\mathbf{k}$  and  $\mathbf{q}$  mesh, we used 8 × 8 × 1. Throughout the manuscript, we used the following convention for spin Hamiltonian,

$$H = - \sum_{i \neq j} \mathbf{e}_i \cdot J_{ij} \cdot \mathbf{e}_j, \quad (1)$$

where  $\mathbf{e}_{i,j}$  refers to the unit spin vectors at the atomic site  $i$  and  $j$ , respectively. Due to the negative sign in the spin Hamiltonian, when  $J_{ij}$  is positive, it favors the FM coupling between the atoms; When  $J_{ij}$  is negative, it favors the AFM coupling between the atoms. As magnetic coupling is computed in momentum space and transformed into real space, all the interatomic site pair interactions can be obtained in a single response calculation.

## III. RESULTS AND DISCUSSIONS

Bulk CrI<sub>3</sub> is in a rhombohedral structure with the  $R\bar{3}$  group symmetry at low temperature; with temperature elevated beyond 210 K, it becomes a monoclinic structure with the  $C2/m$  group symmetry [26, 49]. The two structures also exist in bilayer CrI<sub>3</sub>, and they can be simply treated as two different stacking patterns of CrI<sub>3</sub> layers: commonly referred to as  $R\bar{3}$  and  $C2/m$ , as shown in Figs. 1(a) and 1(b), respectively. In addition, Sivadas *et al.* [23] has found more stacking patterns in bilayer CrI<sub>3</sub> by laterally shifting one layer against the other layer, among which  $R\bar{3}$  (also denoted as AB),  $C2/m$  (also denoted as AB’), and AA stackings are at the minimum points of the energy landscape and energetically stable, as confirmed

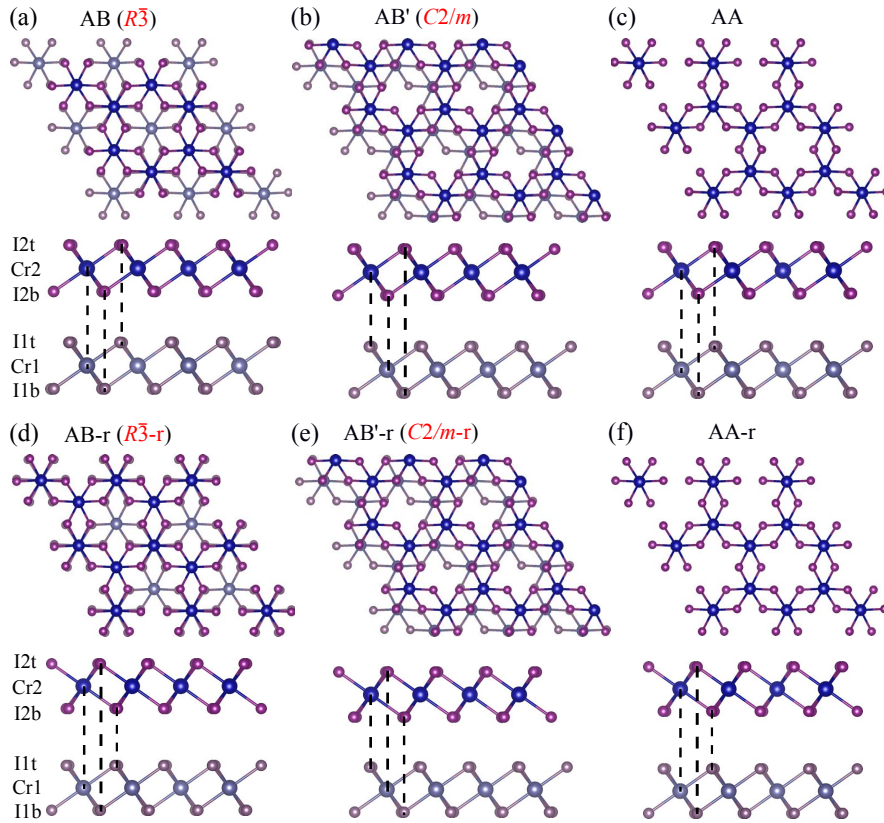


Figure 1. The top and side views of bilayer  $\text{CrI}_3$  with different stacking orders: (a) AB (or  $R\bar{3}$ ), (b)  $\text{AB}'$  (or  $C2/m$ ), and (c) AA, and their  $180^\circ$  rotated counterparts: (d)  $\text{AB-r}$  (or  $R\bar{3-r}$ ), (e)  $\text{AB}'\text{-r}$  (or  $C2/m\text{-r}$ ), and (f)  $\text{AA-r}$ . Cr1(2) indicates the Cr atom in the bottom (top) layer; I1t(b) indicates the I atom in the top (bottom) sublayer in the bottom  $\text{CrI}_3$  layer; I2t(b) indicates the I atom in the top (bottom) sublayer in the top  $\text{CrI}_3$  layer. The dashed lines are for eye guidance of the side view.

by our calculations and illustrated in Figs. 1(a-c). AA stacking indicates that the top and bottom layers are in the same horizontal position. The stacking patterns can be transformed to one another by a relative translation between the two monolayers [23, 49]. By laterally shifting the top layer with  $\frac{2}{3}\vec{a} + \frac{1}{3}\vec{b}$  relative to the bottom layer in AA stacking ( $\vec{a}$  and  $\vec{b}$  are the in-plane lattice vectors), we can obtain AB ( $R\bar{3}$ ) stacking shown in Fig. 1(a). With respect to AB stacking, by translating the top layer with  $\frac{1}{3}\vec{a}$  relative to the bottom layer, we can obtain  $\text{AB}'$  ( $C2/m$ ) stacking shown in Fig. 1(b). Based on these three stacking orders, we then rotated the top layer by  $180^\circ$  with respect to the bottom layer (the center of rotation chosen at the Cr atom in the top layer), which lead to three new energetically stable stacking patterns:  $\text{AB-r}$  ( $R\bar{3-r}$ ),  $\text{AB}'\text{-r}$  ( $C2/m\text{-r}$ ), and  $\text{AA-r}$  shown in Figs. 1(d-f), respectively. It is interesting to note that the normal stackings and their reversed counterparts are difficult to be differentiated from the top view; however, their differences can be seen from the side view. For example, for  $C2/m$  stacking in Fig. 1(b), the I atom in the bottom sublayer of the top  $\text{CrI}_3$  layer (I2b) sits approximately above the Cr atom in the bottom  $\text{CrI}_3$  layer (Cr1), and the I atom in the top sublayer of the top  $\text{CrI}_3$  layer (I2t) sits roughly above the I atom in the bottom sublayer of the bottom  $\text{CrI}_3$  layer (I1b); for  $C2/m\text{-r}$  stacking in Fig. 1(e), the lateral atomic positions ( $x$  and  $y$ ) of I2b and I2t are switched because of the  $180^\circ$

rotation, and therefore I2t sits approximately above Cr1, and I2b sits roughly above I1b. Similar changes are present for the other two stacking orders. Such a rotation-induced change in the atomic alignments between the layers has profound consequences in the magnetic ground state of bilayer  $\text{CrI}_3$  as will be discussed below.

Total energy calculations of bilayer structures in all six stacking patterns ( $R\bar{3}$ ,  $R\bar{3-r}$ ,  $C2/m$ ,  $C2/m\text{-r}$ , AA, and  $\text{AA-r}$ ) were then carried out by considering both interlayer FM and AFM interactions. The results show that the lowest energy state corresponds to  $R\bar{3}$  stacking with the FM order, which is consistent with previous DFT studies [23–25] and demonstrates that the low temperature  $R\bar{3}$  phase has the lowest energy. The shifted energies of all the considered structures with respect to the energy of the FM bilayer at  $R\bar{3}$  stacking are plotted in Fig. 2. As discussed in the Methods section, energy calculations were performed in two different DFT+ $U$  methods: Dudarev’s approach [40] and Liechtenstein’s approach [42], with varying  $U$  and  $J$  values adopted by prior DFT works [23–25]. For Dudarev’s approach shown in Fig. 2(a), when  $U_{eff}$  is relatively small ( $U_{eff} < 3.0$  eV), the AFM bilayer at  $R\bar{3}$  stacking is the second lowest energy state of all the structures. With  $U_{eff}$  increasing ( $U_{eff} \geq 3.0$  eV), the AFM bilayer at  $C2/m$  stacking becomes the second lowest energy state of all the structures, and its energy is lower than that of the FM bilayer

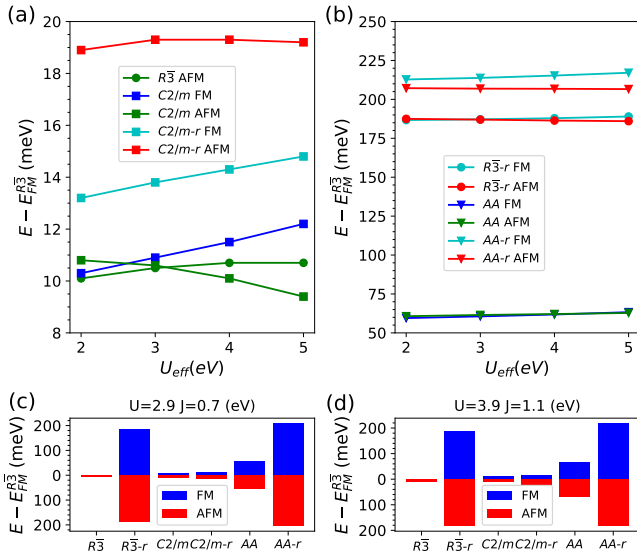


Figure 2. The total energy of bilayer  $\text{CrI}_3$  in all six stacking patterns ( $R\bar{3}$ ,  $R\bar{3}$ -r,  $C2/m$ ,  $C2/m$ -r, AA, and AA-r) with interlayer FM or AFM order.  $R\bar{3}$  stacking with the FM order has the lowest energy and thus was used as the zero energy reference. Data in (a) and (b) were obtained by Dudarev's DFT+ $U$  approach with different  $U_{\text{eff}}$  values, where data with energy below 20 meV is shown in (a) and data with energy above 50 meV is shown in (b). Data in (c) and (d) were obtained by Liechtenstein's DFT+ $U$  approach with (c) $U = 2.9$  eV,  $J = 0.7$  eV, and (d)  $U = 3.9$  eV,  $J = 1.1$  eV.

at  $C2/m$  stacking. This result is not surprising and consistent with previous studies [23–25] as the AFM bilayer at  $C2/m$  stacking is considered to be the magnetic ground state of the high temperature structural phase, while the FM bilayer at  $R\bar{3}$  stacking corresponds to the magnetic ground state of the low temperature phase. Notably, within energy difference of 20 meV with respect to the FM bilayer at  $R\bar{3}$  stacking, there also exist the FM bilayer at  $C2/m$ -r stacking and the AFM bilayer at  $C2/m$ -r stacking, as shown in Fig. 2(a); in contrast, both FM and AFM bilayers at  $R\bar{3}$ -r stacking and all the bilayers at AA and AA-r stackings have energies at least 50 meV above the FM bilayer at  $R\bar{3}$  stacking, as shown in Fig. 2(b). For Liechtenstein's DFT+ $U$  approach, similar results can be observed in Fig. 2(c) with  $U = 2.9$  eV and  $J = 0.7$  eV and Fig. 2(d) with  $U = 3.9$  eV and  $J = 1.1$  eV. Several points can be made from our calculations in Fig. 2: first, for bilayer  $\text{CrI}_3$ ,  $R\bar{3}$  stacking with the FM interlayer magnetic order ( $R\bar{3}$  FM in short) is the most energetically stable, while  $R\bar{3}$  AFM,  $C2/m$  FM,  $C2/m$  AFM,  $C2/m$ -r FM, and  $C2/m$ -r AFM are in the close proximity in the energy landscape; second, although  $R\bar{3}$  stacking is stable, its rotated counterpart  $R\bar{3}$ -r becomes significantly less stable, particularly compared to  $C2/m$  and its rotated counterpart  $C2/m$ -r; third, AA stacking is a metastable stacking order in comparison with  $R\bar{3}$  and  $C2/m$  stackings [23], which explains why it is rarely observed experimentally, and its rotated counterpart AA-r is even less energetically stable. In short, in normal stacking orders,  $R\bar{3}$  and  $C2/m$  can exist and their energy differences are small, as verified by experimen-

tal works [27–30] and theoretical studies [23–25]; after 180° rotation, however, the energy order is switched, where  $C2/m$ -r remains stable while  $R\bar{3}$ -r becomes much less stable. This suggests that stacking reversal can significantly affect the energies of stacking patterns in bilayer  $\text{CrI}_3$ , and even switch the energy order between stackings. To understand why and how stacking reversal affects the total energy, we examined the averaged interlayer distance in bilayer  $\text{CrI}_3$  at different stacking patterns, as shown in Table S1 in the Electronic Supplementary Information. The difference of the interlayer distance between the FM and AFM order for each stacking is small. The difference of the interlayer distance between  $C2/m$  and  $C2/m$ -r is also small. However, the interlayer distance of  $R\bar{3}$ -r is about 0.54~0.57 Å larger than that of  $R\bar{3}$ ; the interlayer distance of AA-r is about 0.47~0.50 Å larger than that of AA. From Fig. 1, we can see that in  $R\bar{3}$ -r and AA-r stackings, the I atom in the bottom sublayer of the top  $\text{CrI}_3$  layer (I2b) sits almost directly above I1t, the I atom in the top sublayer of the bottom  $\text{CrI}_3$  layer. Therefore, the orbitals from I2b and I1t atoms in these two stackings tend to repel each other, and push the top and bottom  $\text{CrI}_3$  layers farther away, compared to their non-rotated stacking counterparts. This explains the larger interlayer distances (above 4.00 Å) for  $R\bar{3}$ -r and AA-r stackings shown in Table S1, and why their total energies are notably higher in comparison with the corresponding non-rotated stacking patterns  $R\bar{3}$  and AA. In contrast, for  $C2/m$ -r stacking, the rotation does not lead to I2b over I1t, and thus the interlayer distance barely changes compared to the non-rotated  $C2/m$  stacking, which explains why  $C2/m$ -r and  $C2/m$  share similar total energies.

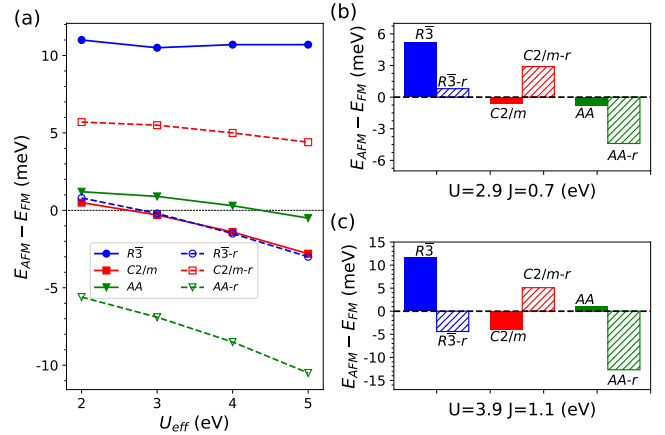


Figure 3. The energy differences between AFM and FM bilayer  $\text{CrI}_3$  at different stacking orders computed by different DFT+ $U$  methods: (a) Dudarev's approach with various  $U_{\text{eff}}$  values; Liechtenstein's approach with (b)  $U = 2.9$  eV and  $J = 0.7$  eV and (c)  $U = 3.9$  eV and  $J = 1.1$  eV.

Now, we move to investigate how the rotation can influence the interlayer magnetic order of each stacking. The energy differences between AFM and FM bilayer  $\text{CrI}_3$  at different stacking patterns ( $R\bar{3}$ ,  $R\bar{3}$ -r,  $C2/m$ ,  $C2/m$ -r, AA and AA-r) were calculated again by different DFT+ $U$  methods with various sets of  $U$  and  $J$  values, as shown in Fig. 3. For  $R\bar{3}$

stacking, all the calculations in Figs. 3(a-c) yield the same magnetic ground state, i.e., interlayer FM. For  $R\bar{3}$ -r stacking, however, the situation becomes more complicated. According to Fig. 3(a), calculations by Dudarev’s approach indicate that when  $U_{eff} = 2.0$  eV,  $E_{AFM} - E_{FM} = 0.8$  meV for  $R\bar{3}$ -r stacking so FM is slightly more stable; with  $U_{eff}$  increasing ( $\geq 3.0$  eV),  $E_{AFM} - E_{FM}$  becomes increasingly negative and thus the interlayer magnetic ground state is switched to AFM. Similar trends are found in the data of Figs. 3(b) and 3(c) computed by Liechtenstein’s approach, where  $U = 2.9$  eV and  $J = 0.7$  eV give FM as the magnetic ground state, while  $U = 3.9$  eV and  $J = 1.1$  eV show AFM as the magnetic ground state for  $R\bar{3}$  stacking. As for  $C2/m$  and  $C2/m$ -r stackings, the opposite behavior occurs: for  $C2/m$ -r stacking, all the calculations in Figs. 3(a-c) confirm interlayer FM as the magnetic ground state; for  $C2/m$  stacking, however, the magnetic ground state once again depends on the choice of interaction parameters. As shown in Fig. 3(a), when  $U_{eff} = 2.0$  eV,  $E_{AFM} - E_{FM} = 0.5$  meV for  $C2/m$  stacking and therefore FM is slightly more stable; with  $U_{eff}$  increasing ( $\geq 3.0$  eV),  $E_{AFM} - E_{FM}$  once again becomes increasingly negative and thus the interlayer magnetic ground state is switched to AFM. Calculations by Liechtenstein’s approach with two sets of  $U$  and  $J$  values in Figs. 3(b) and 3(c) both suggest AFM as the magnetic ground state of  $C2/m$  stacking. Finally, moving to AA and AA-r stackings, Dudarev’s approach in Fig. 3(a) shows that the magnetic ground state of AA stacking could have a transition from FM to AFM when  $U_{eff} = 5.0$  eV. Liechtenstein’s approach determines AFM as the magnetic ground state of AA stacking when  $U = 2.9$  eV and  $J = 0.7$  eV (Fig. 3(b)), while FM as the ground state when  $U = 3.9$  eV and  $J = 1.1$  eV (Fig. 3(c)). In contrast, the magnetic ground state of AA-r stacking is found to be AFM by all the calculations. To summarize, we note that the similar change of the magnetic ground state of  $C2/m$  stacking with the  $U$  value has been reported by previous DFT calculations in Ref. [25]. Here in our work, we found that the magnetic ground states of  $R\bar{3}$ -r and AA stackings are also dependent on the interaction parameters. On the contrary, the other three stacking orders, namely  $R\bar{3}$ ,  $C2/m$ -r, and AA-r, maintain the same magnetic ground state under different  $U$  and  $J$  values.

Our results highlight the importance of choosing the DFT+ $U$  approach with suitable  $U$  and  $J$  values when it comes to computing the energies and determining the magnetic ground state of bilayer  $\text{CrI}_3$ , a system with strong electron correlation effects [23–25]. However, the potential change of the magnetic ground state with  $U$  and  $J$  values brings additional challenges for us to determine how stacking reversal will affect the magnetic ground state. For Dudarev’s approach, we have examined  $U_{eff}$  from 2.0 to 5.0 eV, and  $U_{eff}$  is typically chosen around 3.0 eV in the literature [23, 58]. With  $U_{eff} = 3.0$  or 4.0 eV, it is clear from Fig. 3(a) that the  $180^\circ$  stacking rotation remarkably switches the magnetic ground state of all three stacking orders:  $R\bar{3}$ ,  $C2/m$ , and AA. In specific, the magnetic ground state of  $R\bar{3}$  stacking is changed from FM to AFM when it is reversed to  $R\bar{3}$ -r stacking; the ground state of  $C2/m$  stacking is switched from AFM to FM when it is rotated to  $C2/m$ -r stacking; AA stacking shows an FM-to-

AFM transition after the rotation to AA-r stacking. We expect that  $U_{eff} = 2.0$  eV is too low while  $U_{eff} = 5.0$  eV is too high, which could give rise to unreliable results. For Liechtenstein’s approach with  $U = 3.9$  eV and  $J = 1.1$  eV (the values used by Ref. [25]), the switching of interlayer magnetic order by stacking reversal is also evident for all three stacking patterns, as shown in Fig. 3(c); nevertheless, with  $U = 2.9$  eV and  $J = 0.7$  eV (the values used by Ref. [24]), only  $C2/m$  stacking exhibits a clear switching of the magnetic ground state by stacking reversal, as shown in Fig. 3(b). This renders us difficult to determine whether  $R\bar{3}$  and AA stacking orders should definitely experience the magnetic ground state switching after the  $180^\circ$  rotation. Therefore, we further carried out hybrid functional calculations through the screened Heyd-Scuseria-Ernzerhof hybrid functional (HSE06) method [50, 51] without use of any  $U$  and  $J$  parameters. The HSE06 results are shown in Fig. S1 in the Electronic Supplementary Information, where the  $180^\circ$  stacking rotation switches the magnetic ground state for all three stacking orders, similar to the results from Dudarev’s approach with  $U_{eff} = 3.0$  or 4.0 eV shown in Fig. 3(a), and also consistent with the results from Liechtenstein’s approach with  $U = 3.9$  eV and  $J = 1.1$  eV shown in Fig. 3(c). This confirms that stacking reversal is an effective strategy to switch the interlayer magnetic order in bilayer  $\text{CrI}_3$ .

It is important to note that the switching event for  $C2/m$  stacking exists for different DFT+ $U$  approaches with different  $U$  and  $J$  values and the HSE06 method without use of any  $U$  and  $J$  parameters, demonstrating that our results about  $C2/m$  and  $C2/m$ -r stackings are robust. Fortunately, recent experimental studies by polarization resolved Raman spectroscopy [27–30] verified that exfoliated bilayer  $\text{CrI}_3$  assumes the monoclinic  $C2/m$  stacking. Moreover,  $\text{CrBr}_3$  bilayers with the top and bottom layers aligned and anti-aligned were grown by molecular beam epitaxy, and they were found to have opposite interlayer magnetic orders [32]. These experimental findings further corroborate our calculations on  $C2/m$  and  $C2/m$ -r, where the switching of interlayer magnetic order by stacking reversal is present. Therefore, we focus on  $C2/m$  and  $C2/m$ -r stacking patterns to reveal the microscopic mechanism of the switching in the following discussions.

In order to understand the magnetic interactions and the origin of the magnetic ground state change in bilayer  $\text{CrI}_3$ , we performed MFT calculations [52–54, 56, 57], whose results are summarized in Fig. 4. Fig. 4(a) and 4(b) respectively shows the calculated in-plane ( $J_{in}$ , i.e., intralayer) and out-of-plane exchange couplings ( $J_{out}$ , i.e., interlayer) as a function of the distance between Cr atoms. For the out-of-plane interactions, we presented the values multiplied by coordination number  $N$ ;  $\mathcal{J}_{out} = N \cdot J_{out}$  where  $N = 2, 2, 4, 4, 2$  for the 1st, 2nd, 3rd, 4th, and 5th neighbor interactions between the top-layer and bottom-layer Cr atoms, respectively. The first thing to be noted is that the intralayer exchange couplings ( $J_{in}$ ) are not much changed from  $C2/m$  to  $C2/m$ -r stacking, as shown in Fig. 4(a) where the filled-red and the open-blue symbols are largely overlapped except for the small change found in the first neighbor coupling. It is well expected from the 2D nature of  $\text{CrI}_3$ .

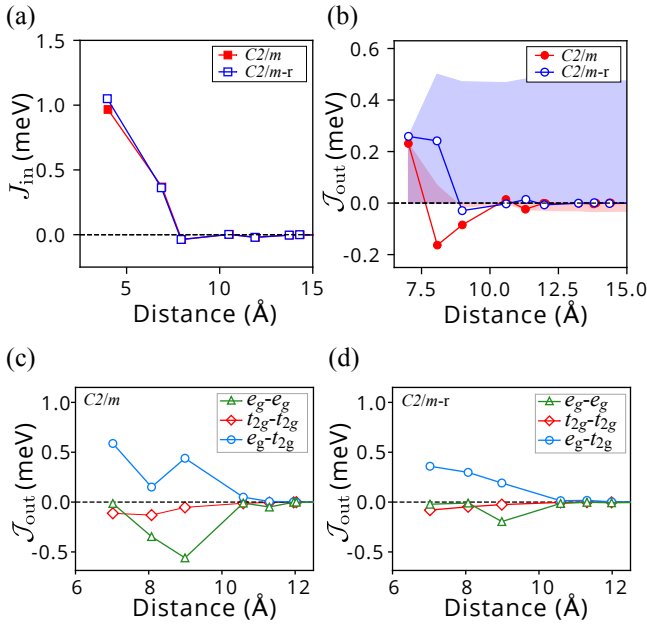


Figure 4. Calculated (a) in-plane and (b) out-of-plane magnetic exchange couplings as a function of the distance between Cr atoms in bilayer  $\text{CrI}_3$ . The filled-red and open-blue symbols represent the results of  $C2/m$  and  $C2/m-r$ , respectively. For the out-of-plane couplings we present the values multiplied by coordination number  $\mathcal{J}_{\text{out}}$  (see the main text). The filled curves (shaded areas) show the integrated values of  $\mathcal{J}_{\text{out}}$  up to the given distance;  $J^{\text{int}}(r) = \sum_0^r \mathcal{J}_{\text{out}}(r)$ . (c), (d) The orbital-decomposed out-of-plane magnetic interactions for  $C2/m$  and  $C2/m-r$  stacking, respectively. The green triangles, red diamonds, and blue circles correspond to the  $e_g-e_g$ ,  $t_{2g}-t_{2g}$  and  $e_g-t_{2g}$  interactions, respectively.

On the other hand, the remarkable difference is clearly noticed in the interlayer couplings. Fig. 4(b) compares the calculated  $\mathcal{J}_{\text{out}}$  in the two different stackings. The key difference is the second neighbor  $\mathcal{J}_{\text{out}}$  whose sign is negative (i.e., favoring the interlayer AFM order) and positive (i.e., favoring the interlayer FM order) in  $C2/m$  and  $C2/m-r$ , respectively. See Eq. 1 in the Methods section to understand why the negative (positive) sign of magnetic couplings favors the AFM (FM) order. While the smaller deviations are found in the longer-range interactions, this second neighbor coupling, as strong as the first neighbor coupling, is certainly the main difference in the two structural phases. The shaded area of Fig. 4(b) refers to the integrated values of all magnetic couplings up to the given distance where red and blue color represents the result of  $C2/m$  and  $C2/m-r$ , respectively. It clearly shows that the AFM (negative sign) and FM (positive sign) interlayer coupling is favored for  $C2/m$  and  $C2/m-r$ , respectively, which is in agreement with our total energy results discussed above. It is interesting to note that, while the major AFM coupling is the second neighbor  $\mathcal{J}_{\text{out}}$ , the longer-ranged AFM couplings, particularly the 3rd and the 5th neighbor interactions, also make critical contributions in stabilizing the interlayer AFM order for the  $C2/m$  phase of bilayer  $\text{CrI}_3$  [24].

Further information can be obtained from the orbital-

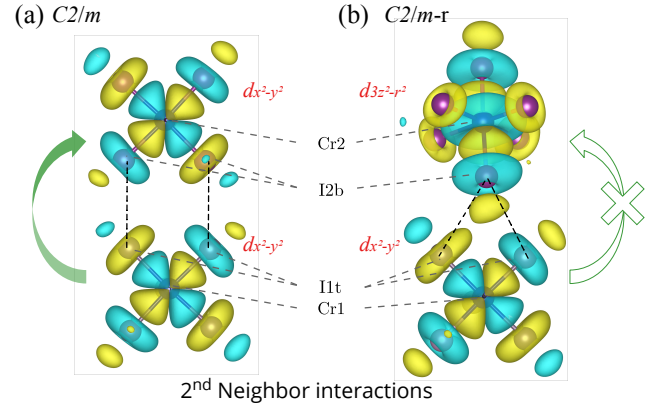


Figure 5. Calculated maximally localized Wannier orbitals mainly responsible for the interlayer  $e_g-e_g$  hopping in (a)  $C2/m$  and (b)  $C2/m-r$  stackings. The dashed lines depict the hopping paths in between the top-layer and bottom-layer I atoms. The blue and yellow colors represent the opposite signs of wavefunction phases.

decomposed interaction profile. It is instructive to compare the result of  $C2/m-r$  presented in Fig. 4(d) with that of  $C2/m$  in Fig. 4(c) which was discussed in the previous study [24]. Just as in  $C2/m$ , the FM interlayer couplings in  $C2/m-r$  are mediated by  $e_g-t_{2g}$  interaction and the AFM by  $e_g-e_g$  and  $t_{2g}-t_{2g}$  interactions. In  $C2/m-r$ , however, the AFM  $e_g-e_g$  coupling is significantly weaker than that in  $C2/m$ . Together with the stronger FM coupling of the second neighbor  $e_g-t_{2g}$ , the interlayer FM order is stabilized in  $C2/m-r$ .

To understand the origin of the weaker second neighbor  $e_g-e_g$  coupling in  $C2/m-r$  stacking, we performed the maximally localized Wannier function (MLWF) analysis and the results are presented in Fig. 5, where the typically large contributions among  $e_g-e_g$  channels are selected for presentation. It shows the wavefunction characters that play the major role in the  $e_g-e_g$  couplings in the two different stacking orders, because the successive hoppings between Cr- $d$  and I- $p$  as well as I- $p$  and I- $p$  are important for the interlayer magnetic interactions [23, 24]. For  $C2/m$  shown in Fig. 5(a) (also for the case of  $R\bar{3}$ , not shown), the two symmetric hopping paths are well identified in between the top-layer and bottom-layer Cr- $e_g$  orbitals. It is consistent with the previous analysis of Ref. [24]. For  $C2/m-r$  shown in Fig. 5(b), on the other hand, the main second neighbor interaction is mediated by two hopping paths and their contributions largely cancel each other owing to the opposite signs of wavefunction phases (see the two dashed lines connecting I atoms in Fig. 5(b): one connects yellow to blue while the other connects blue to blue in terms of wavefunction phases). This effect therefore significantly reduces the AFM  $e_g-e_g$  coupling, which is a distinctive feature not observed in the case of  $C2/m$ , and is largely responsible for the FM ground state in  $C2/m-r$ . Indeed, our tight-binding analysis shows that the  $e_g-e_g$  hopping is about 6 times greater in  $C2/m$  than in  $C2/m-r$ , which is largely attributed to the cancellation due to the wavefunction phases in the latter. To summarize, the  $180^\circ$  stacking rotation from  $C2/m$  to  $C2/m-r$  in bilayer  $\text{CrI}_3$  clearly changes the relative atomic alignments

between the layers, and alters the hopping paths between the top-layer and bottom-layer Cr orbitals, thereby leading to different interlayer magnetic exchange couplings and eventually a different interlayer magnetic ground state. We expect that similar orbital analysis can be applied to bilayer  $\text{CrBr}_3$  to explain the experimentally observed switching of the magnetic ground state by stacking reversal [32].

#### IV. CONCLUSIONS

In conclusion, we carried out extensive first-principles calculations by using different DFT+ $U$  methods with various interaction parameters of  $U$  and  $J$  and by using the hybrid functional method, to investigate the magnetic interactions of three energetically stable stacking patterns  $R\bar{3}$ ,  $C2/m$  and AA in bilayer  $\text{CrI}_3$ , and their corresponding reversed stackings  $R\bar{3}$ -r,  $C2/m$ -r and AA-r. We found that the  $180^\circ$  stacking rotation can significantly affect the total energy and interlayer magnetic ground state. First, stacking reversal changes the energy order between  $R\bar{3}$  and  $C2/m$ , the two most common stacking configurations in bilayer  $\text{CrI}_3$  (i.e.,  $E(R\bar{3}) < E(C2/m)$  while  $E(C2/m\text{-r}) < E(R\bar{3}\text{-r})$ ); second and more interestingly, stacking reversal can switch the interlayer magnetic ground state from FM to AFM for  $R\bar{3}$ , from AFM to FM for  $C2/m$ , and from FM to AFM for AA. A detailed microscopic orbital analysis was also performed by magnetic force theory calculations on  $C2/m$  and  $C2/m$ -r stacking orders to reveal the interlayer magnetic interactions and the origin of the magnetic order change. The  $180^\circ$  stacking rotation changes the relative atomic alignments between the  $\text{CrI}_3$  layers, and alters the hopping paths between the top-layer and bottom-layer Cr orbitals, therefore leading to different interlayer magnetic exchange couplings and eventually a different magnetic ground state. This work demonstrates that stacking rotation, like stacking translation, is also a powerful approach to tune the interlayer magnetism of  $\text{CrI}_3$ . We expect that similar manipulation of the interlayer magnetic order by rotating layers can exist for other 2D magnets such as  $\text{CrBr}_3$  and  $\text{CrCl}_3$ , and magnetic vdW heterostructures.

Furthermore, our findings could exert a broad influence in the Moiré physics of 2D magnets. For example, twisted bilayer  $\text{CrI}_3$  leads to a magnetic Moiré superlattice hosting different local stacking orders corresponding to the translation and rotation of high-symmetry stacking patterns found in the original bilayer structure. More specifically,  $R\bar{3}$ ,  $C2/m$  and AA stacking patterns, as well as another two metastable stackings  $AC'$  and  $AB'_1$ , can be translated to one another, and they have different interlayer magnetic ground states [23]. By twisting bilayer  $\text{CrI}_3$  from the original structure, especially by

a small angle, a Moiré superlattice is formed with a mixture of different local stacking orders [23, 59, 60]. These local stacking orders correspond to  $R\bar{3}$ ,  $C2/m$ , AA,  $AC'$  and  $AB'_1$  stackings, where  $R\bar{3}$  and AA form FM spin centers, while  $C2/m$ ,  $AC'$  and  $AB'_1$  form AFM spin centers in the twisted geometry. Therefore, twisted bilayer  $\text{CrI}_3$  can host different spin centers in the same structure. Our work further shows that stacking rotation can switch the interlayer magnetic order. Hence, by continuing to twist the bilayer structure (i.e., rotating the structure), these localized spin centers are expected to experience the spin flipping, so FM centers become AFM centers while AFM centers become FM centers, resulting in rich and novel magnetic properties in 2D magnetic Moiré superlattices. Finally, when the twist angle is close to  $180^\circ$ , the Moiré superlattice comprises mixed local stacking orders including  $R\bar{3}$ -r,  $C2/m$ -r, AA-r that exhibit the opposite spin behaviors to the twisted structure near  $0^\circ$ .

#### ACKNOWLEDGMENTS

Part of this research was conducted at the Center for Nanophase Materials Sciences, which is a DOE Office of Science User Facility. X. K. and L. L. used resources of the Compute and Data Environment for Science (CADES) at the Oak Ridge National Laboratory, which is supported by the Office of Science of the U.S. Department of Energy under Contract No. DE-AC05-00OR22725. The authors also used resources of the National Energy Research Scientific Computing Center, a DOE Office of Science User Facility supported by the Office of Science of the U.S. DOE under Contract No. DE-AC02-05CH11231. H. K. Yoon and M. J. Han were supported by the Creative Materials Discovery Program through the National Research Foundation of Korea (NRF) funded by the Ministry of Science and ICT and Korea Government (MIST) (Nos. 2018M3D1A1058754 and 2021R1A2C1009303) and the KAIST Grand Challenge 30 Project (KC30) funded by the Ministry of Science and ICT and KAIST, Korea (No. 1711100606/N11190153).

Notice: This manuscript has been authored by UT-Battelle, LLC under Contract No. DE-AC05-00OR22725 with the U.S. Department of Energy. The United States Government retains and the publisher, by accepting the article for publication, acknowledges that the United States Government retains a non-exclusive, paid-up, irrevocable, world-wide license to publish or reproduce the published form of this manuscript, or allow others to do so, for United States Government purposes. The Department of Energy will provide public access to these results of federally sponsored research in accordance with the DOE Public Access Plan (<http://energy.gov/downloads/doi-public-access-plan>).

[1] Kostya S Novoselov, Andre K Geim, Sergei V Morozov, Dingde Jiang, Yanshui Zhang, Sergey V Dubonos, Irina V Grigorieva, and Alexandr A Firsov. Electric field effect in atomically thin carbon films. *science*, 306(5696):666–669, 2004.

[2] A. H. Castro Neto, F. Guinea, N. M. R. Peres, K. S. Novoselov, and A. K. Geim. The electronic properties of graphene. *Rev. Mod. Phys.*, 81:109–162, Jan 2009.

[3] KS Novoselov, o A Mishchenko, o A Carvalho, and AH Castro

- Neto. 2d materials and van der waals heterostructures. *Science*, 353(6298), 2016.
- [4] Je-Geun Park. Opportunities and challenges of 2d magnetic van der waals materials: magnetic graphene? *Journal of Physics Condensed Matter*, 28(30):301001, 2016.
- [5] Bevin Huang, Genevieve Clark, Efrén Navarro-Moratalla, Dahlia R Klein, Ran Cheng, Kyle L Seyler, Ding Zhong, Emma Schmidgall, Michael A McGuire, David H Cobden, et al. Layer-dependent ferromagnetism in a van der waals crystal down to the monolayer limit. *Nature*, 546(7657):270–273, 2017.
- [6] Cheng Gong, Lin Li, Zhenglu Li, Huiwen Ji, Alex Stern, Yang Xia, Ting Cao, Wei Bao, Chenzhe Wang, Yuan Wang, et al. Discovery of intrinsic ferromagnetism in two-dimensional van der waals crystals. *Nature*, 546(7657):265–269, 2017.
- [7] Yujun Deng, Yijun Yu, Yichen Song, Jingzhao Zhang, Nai Zhou Wang, Zeyuan Sun, Yangfan Yi, Yi Zheng Wu, Shiwei Wu, Junyi Zhu, et al. Gate-tunable room-temperature ferromagnetism in two-dimensional fe<sub>3</sub> gete<sub>2</sub>. *Nature*, 563(7729):94–99, 2018.
- [8] Yujun Deng, Yijun Yu, Meng Zhu Shi, Zhongxun Guo, Zihan Xu, Jing Wang, Xian Hui Chen, and Yuanbo Zhang. Quantum anomalous hall effect in intrinsic magnetic topological insulator mnbi<sub>2</sub>te<sub>4</sub>. *Science*, 367(6480):895–900, 2020.
- [9] Soonmin Kang, Kangwon Kim, Beom Hyun Kim, Jonghyeon Kim, Kyung Ik Sim, Jae-Ung Lee, Sungmin Lee, Kisoo Park, Seokhwan Yun, Taehun Kim, et al. Coherent many-body exciton in van der waals antiferromagnet nips<sub>3</sub>. *Nature*, 583(7818):785–789, 2020.
- [10] Kyle Hwangbo, Qi Zhang, Qianni Jiang, Yong Wang, Jordan Fonseca, Chong Wang, Geoffrey M Diederich, Daniel R Gamelin, Di Xiao, Jiun-Haw Chu, et al. Highly anisotropic excitons and multiple phonon bound states in a van der waals antiferromagnetic insulator. *Nature Nanotechnology*, pages 1–6, 2021.
- [11] Xingzhi Wang, Jun Cao, Zhengguang Lu, Arielle Cohen, Hikari Kitadaï, Tianshu Li, Matthew Wilson, Chun Hung Lui, Dmitry Smirnov, Sahar Sharifzadeh, et al. Spin-induced linear polarization of excitonic emission in antiferromagnetic van der waals crystals. *arXiv preprint arXiv:2006.07952*, 2020.
- [12] David Soriano, Mikhail I Katsnelson, and Joaquín Fernández-Rossier. Magnetic two-dimensional chromium trihalides: A theoretical perspective. *Nano Letters*, 20(9):6225–6234, 2020.
- [13] Hailong Lin, Faguang Yan, Ce Hu, Quanshan Lv, Wenkai Zhu, Ziao Wang, Zhongming Wei, Kai Chang, and Kaiyou Wang. Spin-valve effect in fe<sub>3</sub>gete<sub>2</sub>/mos<sub>2</sub>/fe<sub>3</sub>gete<sub>2</sub> van der waals heterostructures. *ACS Applied Materials & Interfaces*, 12(39):43921–43926, 2020.
- [14] Luman Zhang, Xinyu Huang, Hongwei Dai, Mingshan Wang, Hui Cheng, Lei Tong, Zheng Li, Xiaotao Han, Xia Wang, Lei Ye, et al. Proximity-coupling-induced significant enhancement of coercive field and curie temperature in 2d van der waals heterostructures. *Advanced Materials*, 32(38):2002032, 2020.
- [15] Zhe Wang, Deepak Sapkota, Takashi Taniguchi, Kenji Watanabe, David Mandrus, and Alberto F Morpurgo. Tunneling spin valves based on fe<sub>3</sub>gete<sub>2</sub>/hbn/fe<sub>3</sub>gete<sub>2</sub> van der waals heterostructures. *Nano letters*, 18(7):4303–4308, 2018.
- [16] Ce Hu, Dong Zhang, Faguang Yan, Yucai Li, Quanshan Lv, Wenkai Zhu, Zhongming Wei, Kai Chang, and Kaiyou Wang. From two-to multi-state vertical spin valves without spacer layer based on fe<sub>3</sub>gete<sub>2</sub> van der waals homo-junctions. *Science Bulletin*, 65(13):1072–1077, 2020.
- [17] Sultan Albarakati, Cheng Tan, Zhong-Jia Chen, James G Partridge, Guolin Zheng, Lawrence Farrar, Edwin LH Mayes, Matthew R Field, Changgu Lee, Yihao Wang, et al. Antisymmetric magnetoresistance in van der waals fe<sub>3</sub>gete<sub>2</sub>/graphite/fe<sub>3</sub>gete<sub>2</sub> trilayer heterostructures. *Science advances*, 5(7):eaaw0409, 2019.
- [18] Tiancheng Song, Xinghan Cai, Matisse Wei-Yuan Tu, Xiaoou Zhang, Bevin Huang, Nathan P Wilson, Kyle L Seyler, Lin Zhu, Takashi Taniguchi, Kenji Watanabe, et al. Giant tunneling magnetoresistance in spin-filter van der waals heterostructures. *Science*, 360(6394):1214–1218, 2018.
- [19] Shawulienu Kezilebieke, Md Nurul Huda, Viliam Vaño, Markus Aapro, Somesh C Ganguli, Orlando J Silveira, Szczepan Głodzik, Adam S Foster, Teemu Ojanen, and Peter Liljeroth. Topological superconductivity in a designer ferromagnet-superconductor van der waals heterostructure. *arXiv preprint arXiv:2002.02141*, 2020.
- [20] Dahlia R Klein, David MacNeill, Jose L Lado, David Soriano, Efrén Navarro-Moratalla, Kenji Watanabe, Takashi Taniguchi, Soham Manni, Paul Canfield, Joaquín Fernández-Rossier, et al. Probing magnetism in 2d van der waals crystalline insulators via electron tunneling. *Science*, 360(6394):1218–1222, 2018.
- [21] Yujun Zhang, Xiaohua Wu, BingBing Lyu, Minghui Wu, Shixuan Zhao, Junyang Chen, Mengyuan Jia, Chusheng Zhang, Le Wang, Xinwei Wang, et al. Magnetic order-induced polarization anomaly of raman scattering in 2d magnet cri<sub>3</sub>. *Nano letters*, 20(1):729–734, 2019.
- [22] D Soriano, Claudia Cardoso, and Joaquín Fernández-Rossier. Interplay between interlayer exchange and stacking in cri<sub>3</sub> bilayers. *Solid State Communications*, 299:113662, 2019.
- [23] Nikhil Sivadas, Satoshi Okamoto, Xiaodong Xu, Craig J Fennie, and Di Xiao. Stacking-dependent magnetism in bilayer cri<sub>3</sub>. *Nano letters*, 18(12):7658–7664, 2018.
- [24] Seung Woo Jang, Min Yong Jeong, Hongkee Yoon, Siheon Ryeec, and Myung Joon Han. Microscopic understanding of magnetic interactions in bilayer cri<sub>3</sub>. *Phys. Rev. Materials*, 3:031001, Mar 2019.
- [25] Peiheng Jiang, Cong Wang, Dachuan Chen, Zhicheng Zhong, Zhe Yuan, Zhong-Yi Lu, and Wei Ji. Stacking tunable interlayer magnetism in bilayer cri<sub>3</sub>. *Phys. Rev. B*, 99:144401, Apr 2019.
- [26] Michael A McGuire, Hemant Dixit, Valentino R Cooper, and Brian C Sales. Coupling of crystal structure and magnetism in the layered, ferromagnetic insulator cri<sub>3</sub>. *Chemistry of Materials*, 27(2):612–620, 2015.
- [27] Tingxin Li, Shengwei Jiang, Nikhil Sivadas, Zefang Wang, Yang Xu, Daniel Weber, Joshua E Goldberger, Kenji Watanabe, Takashi Taniguchi, Craig J Fennie, et al. Pressure-controlled interlayer magnetism in atomically thin cri<sub>3</sub>. *Nature materials*, 18(12):1303–1308, 2019.
- [28] Tiancheng Song, Zaiyao Fei, Matthew Yankowitz, Zhong Lin, Qianni Jiang, Kyle Hwangbo, Qi Zhang, Bosong Sun, Takashi Taniguchi, Kenji Watanabe, et al. Switching 2d magnetic states via pressure tuning of layer stacking. *Nature materials*, 18(12):1298–1302, 2019.
- [29] Nicolas Ubrig, Zhe Wang, Jérémie Teyssier, Takashi Taniguchi, Kenji Watanabe, Enrico Giannini, Alberto F Morpurgo, and Marco Gibertini. Low-temperature monoclinic layer stacking in atomically thin cri<sub>3</sub> crystals. *2D Materials*, 7(1):015007, 2019.
- [30] Dahlia R Klein, David MacNeill, Qian Song, Daniel T Larson, Shiang Fang, Mingyu Xu, Raquel A Ribeiro, Paul C Canfield, Efthimios Kaxiras, Riccardo Comin, et al. Enhancement of interlayer exchange in an ultrathin two-dimensional magnet. *Nature Physics*, 15(12):1255–1260, 2019.
- [31] Marco Gibertini. Magnetism and stability of all primitive stacking patterns in bilayer chromium trihalides. *Journal of Physics*

- D: Applied Physics*, 54(6):064002, 2020.
- [32] Weijong Chen, Zeyuan Sun, Zhongjie Wang, Lehua Gu, Xiaodong Xu, Shiwei Wu, and Chunlei Gao. Direct observation of van der waals stacking-dependent interlayer magnetism. *Science*, 366(6468):983–987, 2019.
- [33] P. Hohenberg and W. Kohn. Inhomogeneous electron gas. *Phys. Rev.*, 136:B864–B871, Nov 1964.
- [34] G. Kresse and J. Furthmüller. Efficient iterative schemes for ab initio total-energy calculations using a plane-wave basis set. *Phys. Rev. B*, 54:11169–11186, Oct 1996.
- [35] G. Kresse and D. Joubert. From ultrasoft pseudopotentials to the projector augmented-wave method. *Phys. Rev. B*, 59:1758–1775, Jan 1999.
- [36] John P. Perdew, Kieron Burke, and Matthias Ernzerhof. Generalized gradient approximation made simple. *Phys. Rev. Lett.*, 77:3865–3868, Oct 1996.
- [37] Jiří Klimeš, David R. Bowler, and Angelos Michaelides. Van der waals density functionals applied to solids. *Phys. Rev. B*, 83:195131, May 2011.
- [38] Jiří Klimeš, David R Bowler, and Angelos Michaelides. Chemical accuracy for the van der waals density functional. *Journal of Physics: Condensed Matter*, 22(2):022201, 2009.
- [39] Santu Baidya, Jaejun Yu, and Choong H. Kim. Tunable magnetic topological insulating phases in monolayer  $\text{CrI}_3$ . *Phys. Rev. B*, 98:155148, Oct 2018.
- [40] S. L. Dudarev, G. A. Botton, S. Y. Savrasov, C. J. Humphreys, and A. P. Sutton. Electron-energy-loss spectra and the structural stability of nickel oxide: An  $\text{LSDA}+U$  study. *Phys. Rev. B*, 57:1505–1509, Jan 1998.
- [41] V. I. Anisimov, I. V. Solov'yev, M. A. Korotin, M. T. Czyżyk, and G. A. Sawatzky. Density-functional theory and  $\text{NiO}$  photoemission spectra. *Phys. Rev. B*, 48:16929–16934, Dec 1993.
- [42] A. I. Liechtenstein, V. I. Anisimov, and J. Zaanen. Density-functional theory and strong interactions: Orbital ordering in mott-hubbard insulators. *Phys. Rev. B*, 52:R5467–R5470, Aug 1995.
- [43] Siheon Ryee and Myung Joon Han. The effect of double counting, spin density, and hund interaction in the different  $\text{dft}+U$  functionals. *Scientific reports*, 8(1):1–11, 2018.
- [44] T. O. Wehling, E. Şaşıoğlu, C. Friedrich, A. I. Liechtenstein, M. I. Katsnelson, and S. Blügel. Strength of effective coulomb interactions in graphene and graphite. *Phys. Rev. Lett.*, 106:236805, Jun 2011.
- [45] Philipp Werner, Michele Casula, Takashi Miyake, Ferdi Aryasetiawan, Andrew J. Millis, and Silke Biermann. Satellites and large doping and temperature dependence of electronic properties in hole-doped  $\text{BaFe}_2\text{As}_2$ . *Nat. Phys.*, 8(4):331–337, April 2012.
- [46] Youhei Yamaji, Yusuke Nomura, Moyuru Kurita, Ryotaro Arita, and Masatoshi Imada. First-Principles Study of the Honeycomb-Lattice Iridates  $\text{Na}_2\text{IrO}_3$  in the Presence of Strong Spin-Orbit Interaction and Electron Correlations. *Phys. Rev. Lett.*, 113(10):107201, September 2014.
- [47] Seung Woo Jang, Hirofumi Sakakibara, Hiori Kino, Takao Kotani, Kazuhiko Kuroki, and Myung Joon Han. Direct theoretical evidence for weaker correlations in electron-doped and  $\text{Hg}$ -based hole-doped cuprates. *Scientific reports*, 6(1):1–7, 2016.
- [48] Seung Woo Jang, Siheon Ryee, Hongkee Yoon, and Myung Joon Han. Charge density functional plus  $U$  theory of  $\text{LaMnO}_3$ : Phase diagram, electronic structure, and magnetic interaction. *Phys. Rev. B*, 98(12):125126, September 2018.
- [49] Matteo Cococcioni and Stefano de Gironcoli. Linear response approach to the calculation of the effective interaction parameters in the  $\text{LDA}+U$  method. *Phys. Rev. B*, 71:035105, Jan 2005.
- [50] Jochen Heyd, Gustavo E Scuseria, and Matthias Ernzerhof. Hybrid functionals based on a screened coulomb potential. *The Journal of chemical physics*, 118(18):8207–8215, 2003.
- [51] Joachim Paier, Martijn Marsman, K Hummer, Georg Kresse, Iann C Gerber, and Janos G Angyan. Screened hybrid density functionals applied to solids. *The Journal of chemical physics*, 124(15):154709, 2006.
- [52] T. Oguchi, K. Terakura, and A. R. Williams. Band theory of the magnetic interaction in  $\text{MnO}$ ,  $\text{MnS}$ , and  $\text{NiO}$ . *Phys. Rev. B*, 28:6443–6452, Dec 1983.
- [53] A. I. Liechtenstein, M. I. Katsnelson, V. P. Antropov, and V. A. Gubanov. Local spin density functional approach to the theory of exchange interactions in ferromagnetic metals and alloys. *Journal of Magnetism and Magnetic Materials*, 67(1):65–74, 1987.
- [54] Myung Joon Han, Taisuke Ozaki, and Jaejun Yu. Electronic structure, magnetic interactions, and the role of ligands in  $\text{Mn}(n)$  ( $n = 4, 12$ ) single-molecule magnets. *Phys. Rev. B*, 70(18):184421, November 2004.
- [55] <http://www.openmx-square.org/>.
- [56] Hongkee Yoon, Taek Jung Kim, Jae-Hoon Sim, Seung Woo Jang, Taisuke Ozaki, and Myung Joon Han. Reliability and applicability of magnetic-force linear response theory: Numerical parameters, predictability, and orbital resolution. *Phys. Rev. B*, 97(12):125132, March 2018.
- [57] Hongkee Yoon, Taek Jung Kim, Jae-Hoon Sim, and Myung Joon Han. Jx: An open-source software for calculating magnetic interactions based on magnetic force theory. *Comput. Phys. Commun.*, 247:106927, February 2020.
- [58] Junyi Liu, Qiang Sun, Yoshiyuki Kawazoe, and Puru Jena. Exfoliating biocompatible ferromagnetic  $\text{Cr}$ -trihalide monolayers. *Physical Chemistry Chemical Physics*, 18(13):8777–8784, 2016.
- [59] Shengxi Huang, Liangbo Liang, Xi Ling, Alexander A Puretzy, David B Geohegan, Bobby G Sumpter, Jing Kong, Vincent Meunier, and Mildred S Dresselhaus. Low-frequency interlayer raman modes to probe interface of twisted bilayer  $\text{MoS}_2$ . *Nano Letters*, 16(2):1435–1444, 2016.
- [60] Alexander A Puretzy, Liangbo Liang, Xufan Li, Kai Xiao, Bobby G Sumpter, Vincent Meunier, and David B Geohegan. Twisted  $\text{MoS}_2$  bilayers with variable local stacking and interlayer coupling revealed by low-frequency raman spectroscopy. *ACS Nano*, 10(2):2736–2744, 2016.